

Imaging Structural and Electrical Changes of Aging Cells Using Scanning Ion Conductance Microscopy

Yao Song, Shuting Zhang, Chen Cao, Jia Yan, Mei Li, Xinyu Li, Feng Chen,* and Ning Gu*

The local charge density and distribution of extracellular membranes play a crucial role in the various cellular processes, such as regulation and localization of membrane proteins, electrophysiological signal transduction, transcriptional control, cell growth, and cell death. In this study, a novel scanning ion conductance microscopy-based method is employed to extracellular membrane mapping. This method allows to not only visualize the dynamic topography and surface charge distribution around individual cells, but also distinguish the charge difference. To validate the accuracy and effectiveness of this method, the charge density on model sample surfaces are initially manipulated and the charge sensing mechanism using finite element modeling (FEM) is explored subsequently. By applying this method, both the extracellular charge distributions and topography structures of normal and senescent human dental pulp stem cells (hDPSCs) are able to monitor. Interestingly, it is observed that the surface charge became significantly more negative after cellular senescence. This innovative approach enables us to gain valuable insights into surface charge changes during cellular senescence, which can contribute to a better understanding of the underlying mechanisms and potential therapeutic strategies for age-related diseases.

1. Introduction

A comprehensive understanding in the behavior of single cell membranes is essential for basic cellular physiology study and

smart materials design.^[1–3] However, it poses significant challenges due to the complex nature of cellular processes and the need for high-resolution techniques. The surface charge of cellular membrane plays a critical role in numerous dynamic interfacial equilibria and processes. Currently, most cellular imaging studies on cells are limited to the morphology visualization and the expression of specific markers.^[4] By studying and analyzing surface charge, valuable insights can be obtained regarding the functionality of biomolecular assemblies and various biological structures, including cells and tissues.^[5,6] The local charge density and distribution are important yet largely hypothetical parameters, but measuring the local charge of cells has been difficult until recently due to lack of reliable methods at micro-to nanoscale, especially under complex physiological conditions.^[7] Traditionally, the electro-kinetic zeta potential has been the most common method for characterizing

surface charge. However, it only provides a bulk average measurement on samples and cannot capture the local charge distribution on individual cells or subcellular structures,^[8] which restricts the ability to fully understand the intricate electrochemical processes occurring at the cell membrane. Fluorescence microscopy, based on dye-labeling techniques, allows for real-time monitoring of various bioelectric signals at the cellular level. However, its spatial resolution is often insufficient to accurately resolve electric signals and subcellular structures.^[9] Furthermore, accessing the interface with required spatial resolution is challenging for fluorescence microscopic techniques. Although atomic force microscopy (AFM) has the capability to map charge distribution, the high force exerted by the AFM probe inadvertently deforms and even impairs the delicate cellular membrane on occasion, limiting its applicability in studying live cells.^[10]

To better understand the relationship between extracellular membrane and cellular behaviors, it is necessary to obtain detailed information of charge distribution with high spatial and temporal resolution. As a promising scanning technique, scanning ion conductance microscopy (SICM) utilizes an electrolyte-filled nanopipette as scanning probe to monitor ionic current and regulate tip-sample distances.^[11–13] SICM is particularly advantageous for biological applications due to its real non-contact scanning with nanoscale resolution, which allows

Y. Song, S. Zhang, C. Cao, M. Li, F. Chen, N. Gu
Key Laboratory for Bio-Electromagnetic Environment and Advanced
Medical Theranostics, School of biomedical engineering and informatics
Nanjing Medical University
Nanjing 211166, P.R. China
E-mail: chenfeng@njmu.edu.cn; guning@seu.edu.cn

J. Yan
Jiangsu Key Laboratory of Oral Diseases
Nanjing Medical University
Nanjing 210029, P.R. China

X. Li
The first school of clinical medicine
Nanjing Medical University
Nanjing 211166, P.R. China

N. Gu
School of Medicine
Nanjing University
Nanjing 210093, P.R. China

The ORCID identification number(s) for the author(s) of this article can be found under <https://doi.org/10.1002/smt.202301315>

DOI: 10.1002/smt.202301315

for imaging flexible biological samples such as living cells, neurons and others. This technique enables the acquisition of high-resolution topography image of single cell in its native environment, without the need for direct mechanical contact. SICM has been successfully employed to study various cellular activities at the subcellular level, capturing static and dynamic changes of plasma membrane under physiological conditions with a resolution of tens of nanometers.^[14] It has also been revealed that SICM can record membrane structural changes over extended periods of time, providing accurate information regarding the structure and location of protein complexes on membrane.^[15,16] Moreover, by integrating SICM with other techniques, quantitative measurements of various cellular parameters, such as membrane potentials, single channel currents, membrane permeability, and transport of electroactive small molecules can be performed.^[17,18] Electrochemical measurement of cells has gained considerable attention for its ability to uncover cellular physical and chemical characteristics.^[19] The integration of organ/intestine-on-chip platforms with analytical biosensors relies on optical and electrochemical sensor to characterize cellular behavior, intra- and interorgan interfaces.^[20,21] Qian et al demonstrated a label-free method for directly detecting the electrochemistry of CD44 molecules and cancer cells.^[22] In addition to topographical and electrochemical imaging, one significant advancement of SICM is the ability to perform surface charge or potential measurements.^[23] Inspired by previous voltage scanning techniques,^[24] researchers are exploring the use of SICM's robust feedback mechanism to study the local charge and potential distribution of porous membranes. Compared to fluorescence microscopy and AFM-based techniques, SICM can achieve a quantitative surface charge map of living non-labeled cell membranes with higher spatial resolution, without direct physical contact, thereby avoiding cell membrane disturbance.^[17] Unwin et al proposed the first SICM-based method to image surface charge of charged polymer features using distance-modulated mode.^[25] Klausen and coworkers applied SICM combined with a novel algorithm to map surface charge density of lipid bilayers from the height difference with two topography images obtained by opposite biases.^[26] Surface charge is also closely related to surface potential,^[11] and He et al utilized a dual-barrel nanopipette for simultaneous topography and surface potential measurements with hopping mode.^[27] However, the advancement of SICM for studying cellular structure and physiology at the microscopic level is on its early stages. Additional researches and advancements in this field are necessary to fully realize its potential.

Senescence is a cellular state characterized by irreversible proliferative arrest and various structural and electrical alterations, often associated with aging.^[28] It can be induced by various insults, such as telomere attrition, DNA damage, and oncogenic mutations.^[29–31] The regenerative capacity of human tissues relies on the potential of adult stem cells to replace damaged cells or tissues. Accurate identification and discrimination of cells are crucial for effective disease therapy, as most diseases originate and progress at the cellular level.^[32] Therefore, exploring physiological changes during the process of stem cell aging is crucial for understanding the overall aging of organism. Human dental pulp stem cell (hDPSC), located in the pulp tissue of teeth, is a type of mesenchymal stem cell that possesses multilineage differentiation potential.^[33] hDPSCs are

easily obtainable and cultured, making them a favorable model for studying human mesenchymal stem cells. In this study, we simplified the experimental setup by detecting ionic current and demonstrated an effective method capable of directly mapping topography and surface charge distribution on a substrate, including complex surfaces such as living cells. We initially conducted systematic studies using available commercial samples to validate this SICM-based imaging technique, and then performed finite element method (FEM) simulations to confirm the sensing capability of surface charge. With the modified SICM technique, we investigated the extracellular membrane of hDPSCs, providing valuable insights into the morphological and electrical alterations during varied cellular states. Understanding these changes that occur in cellular membrane during aging is crucial for unraveling the underlying mechanisms of aging with age-related diseases and thus developing potential interventions.

2. Results and Discussion

2.1. Ionic Current Measurement

By regulating the distance between scanning probe and sample surface (D_{ps}), SICM operates to capture high-resolution topographic images. A glass or quartz pipette with sub-micro/nano-scale opening is filled with electrolyte solution and used as the scanning probe.^[11] Figure 1a illustrates the system for synchronous measurement of topography and current, and a single-barrel glass nanopipette was manufactured and used as scanning probe. The SEM image in Figure 1b displays the side view of nanopipette tip, which has a diameter of ≈ 70 nm. In the circuit depicted in Figure 1c, variable R_{ac} (resistance between nanopipette and sample) is connected in series with constant R_p (resistance of nanopipette), which is determined by the nanopipette geometry. As the nanopipette approaches the sample surface, the ionic current in circuit is affected due to an increase in R_{ac} caused by hindered ion flow at a smaller D_{ps} . The interaction between ionic current and sample surface is complex and depends on factors such as the bias polarity and mode, as well as the electrochemical properties, conductance, and charge of sample.^[25] The glass nanopipette possesses a negatively charged surface in liquid solutions, resulting in electrostatic repulsion when in contact with negatively charged substrate. Conversely, it experiences electrostatic attraction when in contact with substrate with positive charge, which causes less noticeable changes in current.

To mitigate the impact of uneven morphology, available commercial polydimethylsiloxane (PDMS) was employed as model samples. PDMS was chosen due to its odorless nature and low stiffness, which closely resembled the cellular surface.^[34] PDMS is a widely used biomaterial in cell and tissue studies and can be chemically modified to suit specific requirements.^[35] On the commercial PDMS surfaces, modifications were applied using 3-aminopropyltriethoxysilane (APTES), glutaric dialdehyde (GLU), and bovine serum albumin (BSA).^[10] These modifications introduce surface charge differences without altering the surface topography, and the surface roughness ratios of modified surfaces are presented in section 2.3. To validate the relationship between ionic current and surface charge, approaching curves were recorded for diverse charged commercial PDMS substrates.

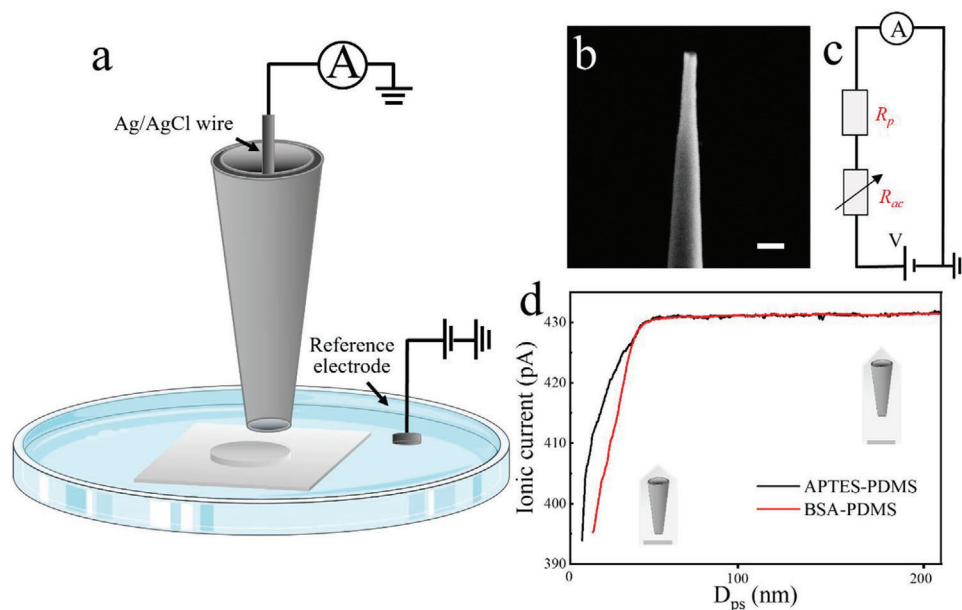


Figure 1. Simultaneous topography and surface charge mapping performed with the ΔI -SICM method. a) Diagram illustrating the ΔI -SICM configuration utilizing a single-barrel glass nanopipette as probe. b) SEM images showing side view (scale bar 1 μm) of a typical SICM nanopipette tip. c) The equivalent circuit for ionic current measurement. d) Obtained approach curves for ionic current on APTES-PDMS (black curve) and BSA-PDMS (red curve) substrates in a PBS solution.

These curves in Figure 1d represent the variation of ionic current as the scanning probe moves closer to substrate surface. A stable electric bias of +0.1 V was applied in the bath, and when nanopipette was positioned far charged surface, the magnitude and phase of oscillating ionic current remained consistent at stable finite values, unaffected by D_{ps} . As the tip approached substrate at an incrementally increasing speed, a significant drop in current was observed over the substrate. It is worth notice that the minimum D_{ps} ($D_{\text{ps-min}}$) changed slightly because the current at $D_{\text{ps-min}}$ was influenced by the surface charge. The general observation from these experiments is that the measured ionic current depends on the charge present on substrate. This small current difference in D_{ps} can be utilized to create surface charge mapping. Further details about the imaging method can be found in experimental section, and the mechanism behind ionic current sensing will be discussed in next chapter.

2.2. Finite Element Methods (FEM) Simulations

It was crucial to evaluate what the nanopipette tip measures from charged surface and determine the region where the tip is most sensitive to substrate surface. To gain insight into the experimental approaching curves, the distributions of electric potential, electric field, and ions transport were investigated using the FEM to solve Poisson-Nernst-Planck (PNP) equations. The FEM provides a powerful framework for studying ionic current response as the scanning nanoprobe is positioned at distinct separations from diverse charged substrates. We employed a 2D axial symmetry in model geometry and assumed a steady state, as shown in Figure S2 (Supporting Information), with 3D view provided in inset i). The quasi-2D view near the tip is shown in inset ii). Dur-

ing simulation, the entire computational domain was discretized into triangular elements (inset (iii)), and rigorous mesh refinements were employed. The position of simulated sample bottom, which includes charged substrates (xa in Figure S2, Supporting Information with surface charge densities of -10 , -20 , and -30 mC m^{-2}) and applied potential region (bc in Figure S2, Supporting Information), varies along the z-axis. The potential gradually reaches zero deep inside nanopipette barrel, with a potential of +0.1 V in bath solution. While we made certain simplifications in simulation system by ignoring the finite size of ions and water, as well as the contribution of electroosmosis, the results still captured main characteristics of experimental changes in current and aided in understand the sensing mechanism. The simulation results depicted in Figure S3 (Supporting Information) demonstrate that the D_{ps} changes can alter the local distribution of electric potential, electric field, and ion flux near the nanopipette tip.

The charge density and D_{ps} were varied in simulations. Figure 2a illustrates the concentration and flux of anions/cations through scanning probe. The surface-dependent ionic current originates from the interplay between mass transport inside and outside nanopipette and the diffuse double layer (DDL) formed at the nanopipette tip and substrate. When the nanopipette tip carries negative charge in bulk solution, the DDLs formed at the nanopipette walls create a perm-selective region, where the migration and diffusion of ions dominate.^[25] The conical geometry of nanopipette limits mass transport inside, while the outer space near the tip allows for faster transport due to a larger access angle.^[5] In Figures 2b, the distribution of electric potential and the direction and distribution of electric field are shown as the tip approaches diverse charged substrates at $D_{\text{ps}} = 30 \text{ nm}$. Consequently, a slight surface-mediated enhance-

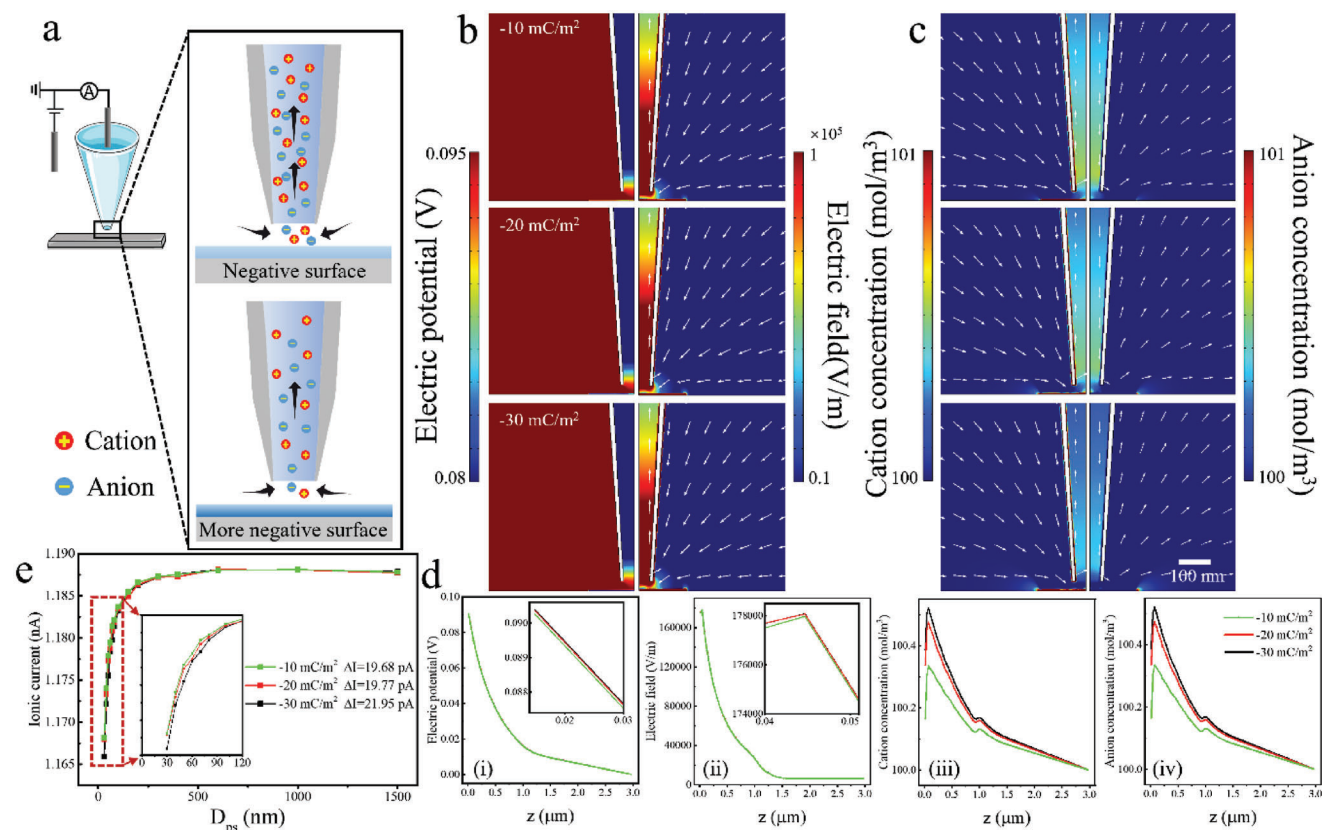


Figure 2. FEM simulations of electric potential, electric field, cation concentration and anion concentration distribution near the tip of nanopipette over -10 , and -20 , -30 mC m^{-2} charged surface at $D_{\text{ps}} = 30$ nm. a) Schematics illustrating the concentration and flux of anions/cations through the SICM nanopipette. b) Electric potential (left column) and electric field (right column) over various charged surface. c) Cation (left column) and anion (right column) concentration over diverse charged surface. d) Distributions of electric potential i), electric field ii), cation concentration iii), and anion concentration iv) along the red dash line showing in Figure S2 (Supporting Information). e) Variation in ionic current change versus D_{ps} on substrates with different charge densities.

ment of the local electric potential occurs over more negatively charged surfaces, while a surface-mediated decrease in the electric field is expected over less negatively charged surfaces, as compared in Figure 2d-i,ii). In Figure 2c,d-iii,iv), the direction and distribution of ion are depicted. In one simulation, the distributions of ions exhibit slight differences, but the orientations are opposite. As the nanopipette approaches charged substrates, the system exhibits perm-selective behavior toward cations or anions depending on the charge density. When the simulated surface carries diverse negative charge, the interface selectivity leads to the accumulation or depletion of ions not only inside the nanopipette but also in a perm-selective zone between the end of nanopipette and the surface. These discontinuous regions in Figure 2d are mainly attributed to the nanoprobe structure's discontinuity. As shown in Figure 2e, the simulated approaching curves were plotted as measured current versus D_{ps} on substrates with different charge densities. The simulation results reveal that the current difference (ΔI , between the closest and farthest points from substrate) over a more negative charged substrate has a larger value. This trend aligns with the experimental results depicted in Figure 1d and confirms that the current magnitude correlates with surface charge density. The simulated current becomes more negative as D_{ps} decreases, and it can be influenced

by the substrate surface charge up to a D_{ps} of ≈ 200 nm. However, the magnitude of ΔI over less negatively charged surface shows a less pronounced contrast compared to more negative surface.

2.3. Surface Charge Mapping by Ionic Current Measurement

SICM, using a pixel-wise mapping method different from fluorescence technique, is operated line by line. However, it is important to note that the simplified current-distance equation shown in Figure 1c is only valid under certain conditions that are commonly used for mapping. When a nanopipette comes close to samples in an electrolyte solution, the ionic current flowing through the nanopipette is influenced by the surface charge of sample. This interaction between current and charged surface can be used to characterize the surface properties. This sensitivity allows SICM to not only perform topography imaging of scanned substrate but also map surface charge. To avoid lateral collisions between nanopipette tip and substrate, especially at steep sides, the skip and ARS dual modes are commonly employed. In the skip mode, the ΔI -based SICM system first performs a coarse scan (typically with 64 points) to assess the overall surface height

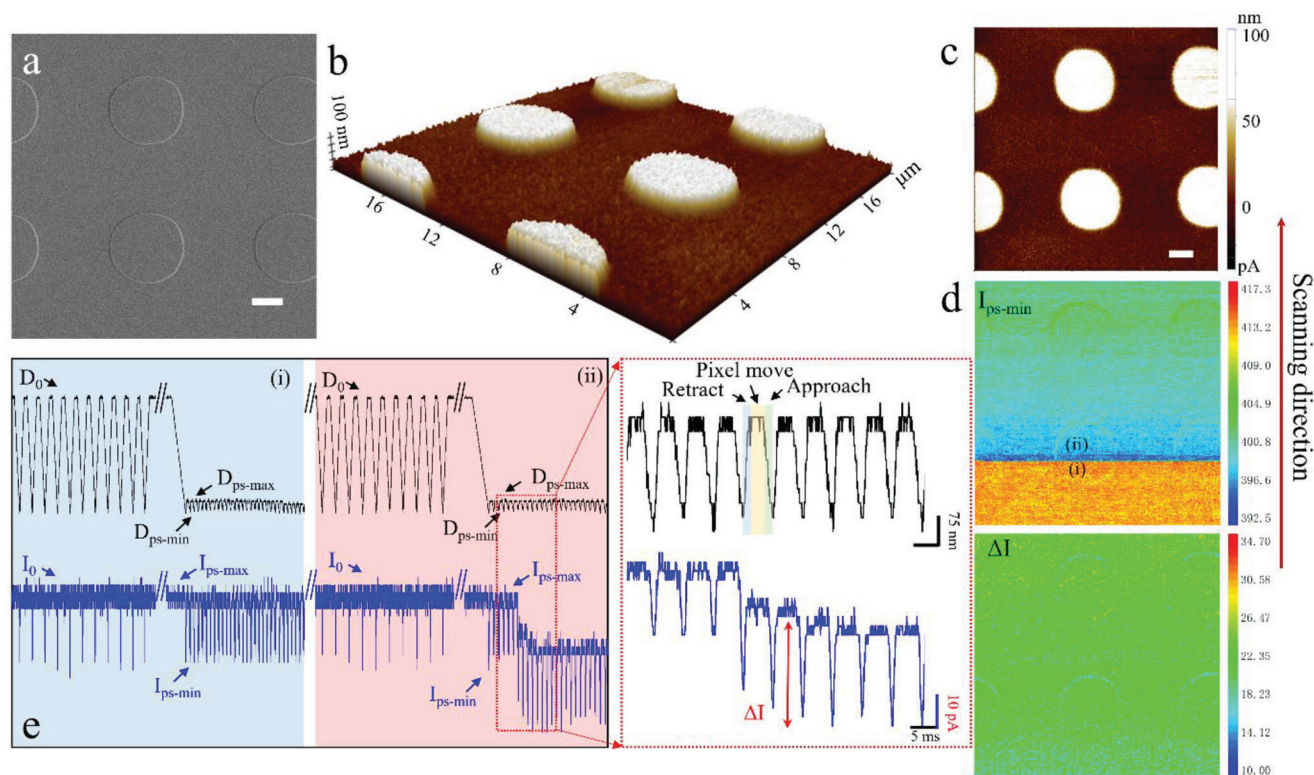


Figure 3. Simultaneous recording topography and surface charge (ΔI) images of APTES-PDMS substrate. a,b) The SEM and 3D topography images (scar bar: 2 μm). c,d) The 2D topography and corresponding ionic current ($I_{\text{ps-min}}$ and ΔI) images (scar bar: 2 μm). e) The time traces of nanopipette movement (D , black) and ionic current variation (I , blue) labeled as i and ii in $I_{\text{ps-min}}$ image.

variation, and then a fine scan (typically with 256 points) is carried out. For complicated surfaces, the ARS mode is suitable as it provides precise control of the nanopipette movement. In this mode, the nanopipette tip approaches the substrate from an initial position, $D_{\text{ps-max}}$, with several microns, and stops at $D_{\text{ps-min}}$ when the current reduction exceeds a predefined set-point (usually 2%). After reaching $D_{\text{ps-min}}$, the ionic current is measured and linked with position information. Subsequently, the nanopipette withdraws from $D_{\text{ps-min}}$ and returns to $D_{\text{ps-max}}$. In addition to maintaining a constant approach speed and a 2% current reduction as the setpoint, the approach step includes a 1% mid-setpoint. At this mid-setpoint, the nanopipette is slightly raised and then continues approaching the sample at half of the original speed.

Figures 3a–c depict the SEM, 3D, and 2D topographic images, respectively, obtained from APTES-PDMS substrate. The 3D topography provides a visual representation of significant height changes across substrate, while the 2D topography offers a more detailed view of local height differences in a $20 \times 20 \mu\text{m}^2$ area. Figure 3d presents the corresponding ionic current images ($I_{\text{ps-min}}$ and ΔI) in heatmap formats. To explain the principle of ΔI mapping, the time traces of nanopipette movement (D) and ionic current (I) from two selected sites, labeled as i and ii in $I_{\text{ps-min}}$ image, are shown in Figure 3e. In each pixel, the nanopipette gradually approaches the surface with a continuously decreasing percentage, followed by a quick retraction to its original position, and then moves laterally to the next pixel (represented by the

black-colored time trace). Throughout the controlled movement of nanopipette, the ionic current (indicated by the blue trace) is applied as feedback to position the nanopipette and recorded for image construction. During imaging process, the initial ionic current at $D_{\text{ps-max}}$ from surface is inevitably influenced by environmental interference, leading to inconsistencies and inaccuracies in current signal at $D_{\text{ps-min}}$. Therefore, it is asserted that the $D_{\text{ps-min}}$ current cannot be employed as a reliable indicator of substrate's surface response. To address this, ΔI is defined as the absolute value of current difference between $D_{\text{ps-min}}$ and $D_{\text{ps-max}}$ in each approach/withdraw cycle. The surface charge map constructed using ΔI is robust against random noise and ion current baseline drift.

2.4. Topography and Surface Charge Mapping of Modified PDMS Substrates

To evaluate the efficacy of ΔI -based SICM method, systematic studies were performed by acquiring topography and ΔI images of modified PDMS substrates. Figure 4a–c show the results of topography and ΔI of APTES- a), GLU- b), and BSA- c) modified PDMS substrates. These topography images match well with the typical one recorded by SEM shown in Figure 3a. The surface topography roughness of modified PDMS substrates were quantified using mean surface area ratio, which were determined to be ≈ 22.416 , 22.549 , and 22.325 nm in a $20 \times 20 \mu\text{m}^2$

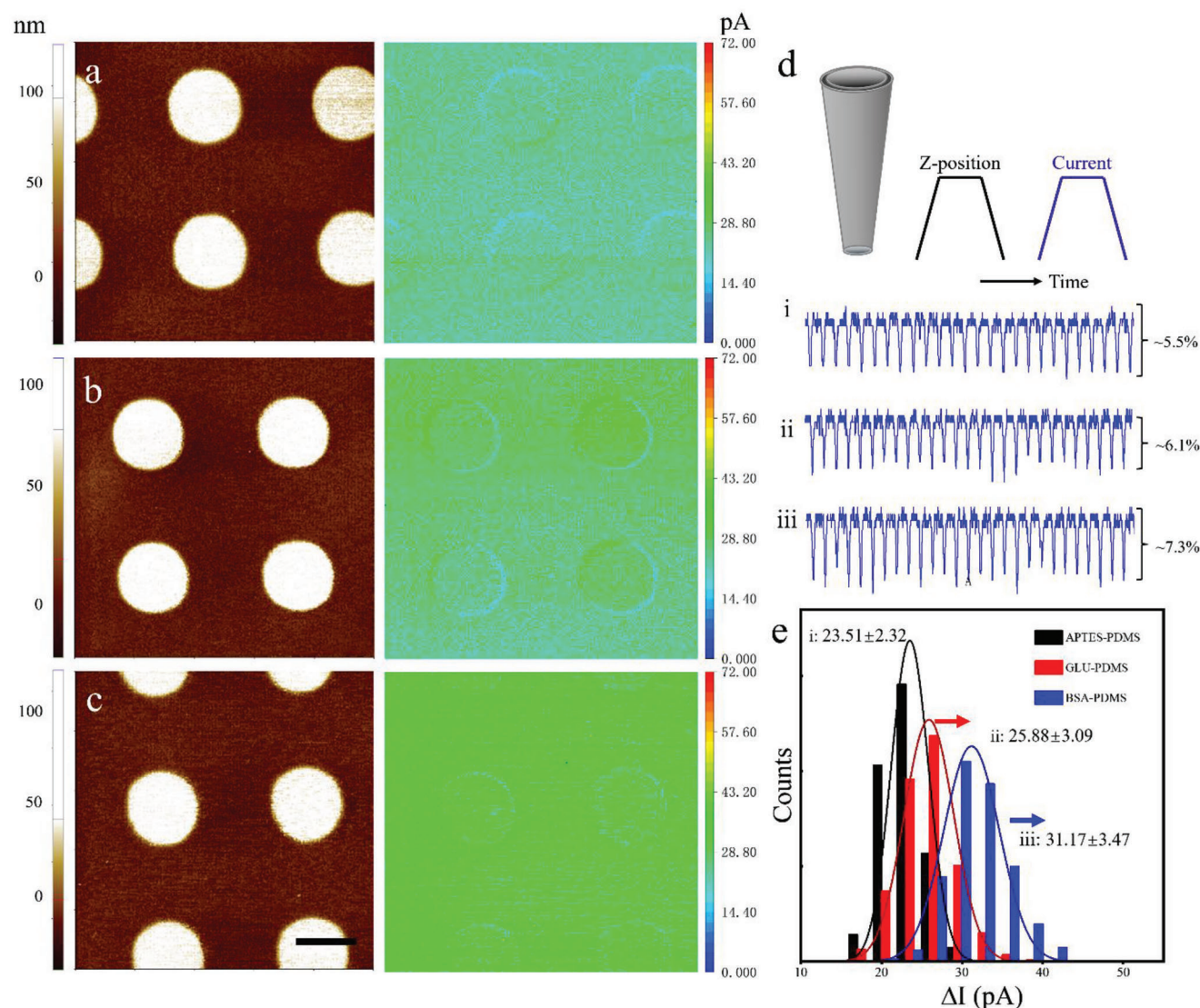
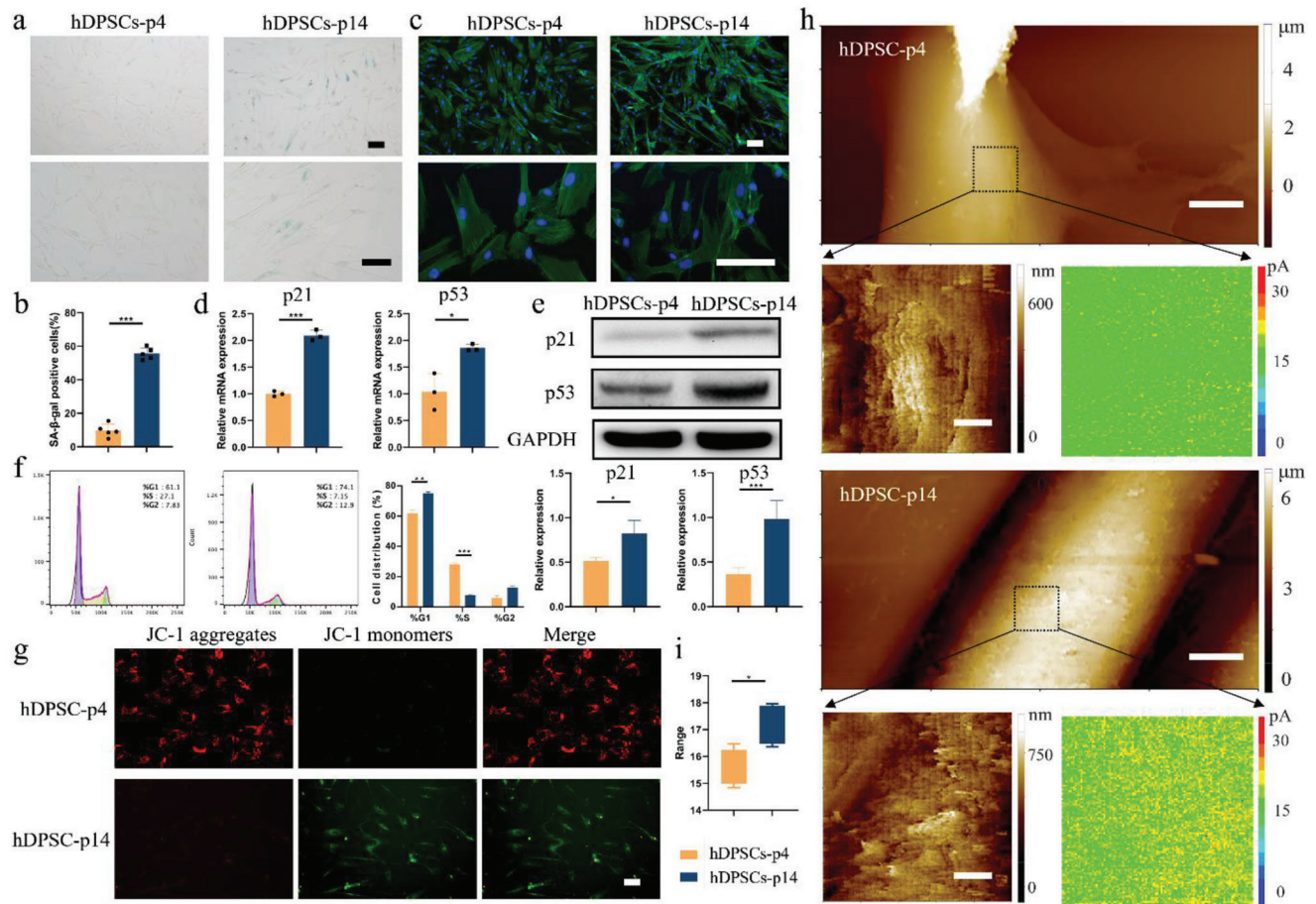


Figure 4. Representative topography and surface charge (ΔI) images of PDMS substrates modified with APTES a), GLU b), and BSA c) molecules (scale bar: 4 μm). d,e) Proportions of current decrease and histograms of ΔI on APTES-PDMS i), GLU-PDMS ii), and BSA-PDMS iii) substrates.

area, respectively. These results confirmed that the modifications did not alter the surface morphology. The nanopipette was gradually brought closer to APTES-PDMS substrate until the fine current drop reached $\approx 5.5\%$ in Figure 4d.i. For GLU- and BSA-PDMS substrates, the nanopipette was approached until the fine current drop percentages reached $\approx 6.1\%$ and 7.3% , respectively, as depicted in Figure 4d.ii,iii. As shown in Figure 4e, the shifts observed in the ΔI histograms of GLU- and BSA-PDMS substrates are noticeable, indicating distinct surface electrical characteristics, which are consistent with the surface zeta potential calculations shown in Figure S4b (Supporting Information). Despite these differences, the main features and surface roughness of substrates appear to be similar. By excluding the influence of inconsistent morphology, we confirmed that the topography and charge distribution of soft sample can be detected and analyzed simultaneously using this ΔI -based SICM method.

2.5. Mapping of Aging Cells

Cellular aging is a complex process influenced by both environmental and endogenous factors, which can be defined as a combination of cell cycle arrest and stereotypical phenotypic changes.^[36] The interplay between mechanical, morphological, and other factors has been found to play a significant role in driving various complex community behaviors.^[37] In previous studies involving primary stem cell extraction, the isolation and culture of stem cells from elderly donors often yield suboptimal results.^[38] The limited proliferative capacity of primary stem cell makes it a suitable system for studying stem cell aging.^[39] In our research, we classified hDPSCs that have undergone 12 or more passages as aging cells, based on decreased proliferation rate and observable morphological changes. To assess cellular senescence, we performed senescence-associated β -galactosidase (SA- β -gal) staining, a widely used marker for senescent cells. **Figure 5a,b**



demonstrate a significant increase in the proportion of senescent cells after passage 14 (hDPSCs-p14) compared to normal cells in passage 3–5 (hDPSCs-p4). Figure 5c reveals noticeable differences in cell morphology and cytoskeletal organization between young and aging cells by cellular cytoskeleton staining. In young cells, the cytoskeleton appeared well-defined and organized, whereas in aging cells, the cytoskeleton became disordered and chaotic. To further confirm the aging process, we examined the expression of aging-related mRNA and proteins.^[36] Figure 5d shows a significant increase in the mRNA expression of p53 and p21 in hDPSCs-p14, which was also reflected in protein expression in Figure 5e. Figure 5f demonstrates a significant increase in the proportion of aged hDPSCs in G1 phase, accompanied by a decrease in S phase, which are associated with the characteristics of cell senescence. These alterations in the cell cycle may be related to abnormalities in intracellular signaling pathways, telomere shortening, accumulation of DNA damage, and other factors.^[40] JC-1 staining was utilized to assess mitochondrial membrane potential. Cells showing high mitochondrial mem-

brane potential displayed aggregated red fluorescence of JC-1, whereas cells with low membrane potential exhibited diffuse green fluorescence. We observed that aging cells displayed stronger green fluorescence in Figure 5g, indicating a lower mitochondrial membrane potential associated with aging.

Cell surface charge is a distinct phenomenon from transmembrane potential, which is an electro-diffusional voltage resulting from variations in inorganic ion concentrations and permeabilities across membrane.^[41] The net electric field at membrane surfaces is influenced by both anionic and cationic functional groups present in the lipid headgroups. Here, we investigated whether this method could be utilized to simultaneously probe the topography and extracellular charge distribution of live cell. hDPSCs were cultured on a transparent gelatin matrix-modified PDMS substrate, which allows for visualization using a bright field optical microscope during SICM experiments and provides a favorable local environment for the hDPSCs growth. Figure 5h shows the 2D topography and ΔI, respectively, of hDPSCs (-p4 and -p14) attached on gelatin matrix support. Both images clearly

depict the microvilli features on cell surface and the fiber network of gelatin-supporting matrix. The membrane pattern of hDPSCs-p4 appears relatively smooth, with a height reaching up to 5 μm . Therefore, the dual modes of SICM in our study demonstrate the capability to accurately capture high spatial resolution topography of intricately shaped living cell surfaces, as well as soft surfaces like the gelatin matrix. Figure 5h,i highlight more negative surface charge of hDPSCs-p14 compared with hDPSCs-p4, suggesting biochemical alterations within aging cells. The regions with high ΔI values may correspond to specific locations of essential proteins in the cell membrane that are known to facilitate fatty acid uptake and other essential functions. These charge differences provide evidence of physiological functional disparities between aging stem cells and normal cells. It is important to note that the surface properties of aging cells, including morphology and charge distribution, may vary depending on cell type, individual differences, and other factors during the aging process.

To investigate the underlying aging mechanisms, we stimulated hDPSCs aging with H_2O_2 .^[42,43] Cellular stimulation with H_2O_2 induces oxidative stress, leading to the generation of excessive reactive oxygen species (ROS) and subsequent cell damage and aging, which is a common model for inducing cellular aging. In this study, we exposed hDPSCs to various concentrations of H_2O_2 to assess the potential toxic effects. Through the cell counting kit-8 (CCK-8) assay, we determined that the optimal concentration for H_2O_2 stimulation was 100 μM in Figure S6a (Supporting Information). After treated for 2 h, followed by a switch to normal culture medium for at least 48 h, positive SA- β -gal staining indicated a successful induction of cellular aging, as shown in Figure S6b (Supporting Information). Following stimulation, the protein expression of p21 and p53 was noticeably elevated (Figure S6c, Supporting Information). It was observed that H_2O_2 -induced aging cells did not exhibit distinct differences in cytoskeletal organization compared to normal cells (Figure S6d, Supporting Information), and no significant differences in surface charge were observed (Figure S6e,f, Supporting Information). We speculated that the aging induced by H_2O_2 stimulation, compared to replicative aging, has a shorter overall cellular lifespan and a singular stimulus, which allows the cells to reach a relatively stable state after the aging stimulus. Thus, the markers of aging can only serve as one form of aging monitoring, as real aging is a complex process involving alterations in the overall cellular membrane. In our study, we observed a difference in surface charge between normal and aging cells, which may be attributed to the electrostatic properties change on cellular membrane. However, further investigation is required to fully understand how these differences correlate with the functional variances observed in aging stem cells.

3. Conclusion

The combination of high-resolution topography imaging and extracellular charge measuring provides valuable insights into the underlying mechanisms of cellular aging. The ΔI -SICM method for extracellular membrane imaging provides an exciting approach to investigating local electrostatic changes in live cell membranes with sub-100 nm spatial resolution. This resolution level is challenging to achieve with conventional electrophysiology methods and emerging voltage-sensitive fluorescence imag-

ing techniques. In conclusion, our study highlights the importance of surface charge in cellular senescence and demonstrates the utility of the SICM-based method for investigating extracellular membrane properties. The observed increase in negative surface charge during cellular senescence suggests alterations in the composition and functionality of cell membrane.

4. Experimental section

Materials and Buffer Solutions: All chemicals were purchased from Sigma Aldrich, unless otherwise specified. The commercial PDMS substrates were obtained from Suzhou Jiutao Sensing Technology. Phosphate buffered saline (PBS) was purchased from Fisher Chemical and used as the standard electrolyte solution for the modified PDMS measurement.

Zeta Potentials of Solid PDMS Films

The zeta potentials of solid PDMS films were measured in a 0.1 mM KCl standard solution.^[44] The modified PDMS layers, ≈ 2 mm thick, were cut into 1×2 cm pieces. These PDMS pieces were immediately stuck on the bottom of a liquid cell (SurPASS III, Anton) by double-sided adhesive tape and then immersed into electrolyte solutions. The KCl standard electrolyte was placed at specific positions, and the pH electrode, conductivity meter, and reference electrode were accurately inserted into the solution. This test involved a comprehensive pH range from 3 to 10.

Human Dental Pulp Stem Cells (hDPSCs) Isolation, Culture, and Identification

Healthy third molars were extracted from patients aged between 15 and 26. The acquisition of clinical-grade hDPSCs has obtained ethical approval from the Ethics Committee of Nanjing Medical University Affiliated Stomatological Hospital (Approval No.: PJ2022-130-001). The samples were rinsed multiple times with ice-cold PBS solution containing 100 U mL^{-1} penicillin/streptomycin (P/S). To access the pulp chamber, sterilized dental fissure burs were used after cleaning the cementum-enamel junction. The pulp tissue was then meticulously separated from the crown and root. A solution of 3 mg mL^{-1} collagenase type I and 4 mg mL^{-1} dispase was employed to digest the pulp tissue for 1 h at 37 $^{\circ}\text{C}$. hDPSCs were cultured in a 5% CO_2 incubator at 37 $^{\circ}\text{C}$ using α -modified Eagle's medium (α -MEM; Gibco) supplemented with 20% fetal bovine serum (FBS; Gibco) and 1% penicillin/streptomycin (P/S). The medium was refreshed on day 6 and every 3 days thereafter. Flow cytometry was conducted according to standard protocols to identify DPSCs. The surface markers were detected in mesenchymal stem cells at passage three with a mesenchymal stem cell (human) surface marker detection kit (Oricell). The data were analyzed using FlowJo 10 software (Tree Star Inc.).

SA- β -Gal Activity Assessment: SA- β -gal staining was conducted using an SA- β -gal kit (cat. no. 9860, Cell Signaling Technology, Inc.) to confirm cellular senescence. At room temperature, the cells were fixed in 4% paraformaldehyde for 10–15 min, followed by two to three washes with PBS. Subsequently, the cells were stained with the staining solution overnight at a final pH of 6.0. The SA- β -gal positive cells were stained blue and quantitatively analyzed using differential interference microscopy (magnification, $\times 100$; analyzing five fields of view per sample). This process was repeated three times for each experimental group.

Immunofluorescence

The cells underwent a 15 min fixation, followed by permeabilization using 0.2% Triton X-100. Subsequently, they were treated with a blocking buffer containing 10% BSA in PBS. Finally, the cells were incubated overnight with a diluted (1:400) CoraLitePlus 488-conjugated Phalloidin antibody (Proteintech). The nuclei were counterstained with DAPI. Mitochondrial membrane potential was detected with the enhanced mitochondrial membrane potential assay kit with JC-1 (Beyotime Biotechnology) following the manufacturer's instructions.

Quantitative Real-Time PCR (qPCR) Analysis

According to the manufacturer's instructions, RNA extraction was performed from cultured hDPSCs using TRIzol reagent (Life Technologies, CA, USA). Complementary DNA (cDNA) synthesis was carried out in a

10 μ L reaction volume using 2 μ g total RNA and PrimeScript reverse transcription master mix (TaKaRa). Quantitative real-time PCR was conducted on an ABI 7900 system (Applied Biosystems, USA) using SYBR Green Premix Ex Taq (TaKaRa). Supplementary Table S2 provides a list of all primer sequences used. Gapdh expression was used for data normalization. The $2^{-\Delta\Delta CT}$ method was employed for quantification of qPCR results.

Western Blot Analysis

Protein extraction from hDPSCs was performed by lysing them with radioimmunoprecipitation assay (RIPA) buffer (Santa Cruz). Following that, the proteins underwent separation via sodium dodecyl sulfate-polyacrylamide gel electrophoresis (SDS-PAGE) on a 10% gel before being transferred onto PVDF membranes (Millipore). The membranes were then incubated overnight with primary antibodies targeting p21 (1:1000, CST), p53 (1:1000, CST), or GAPDH (1:2000, CST). Subsequently, horseradish peroxidase-conjugated secondary antibodies (Shengxing Biological) were applied to the membranes, followed by visualization using enhanced chemiluminescence (Millipore).

SICM Topography and Extracellular Surface Charge Mapping

The PDMS substrate was sterilized using autoclave and then incubated with a 0.1% gelatin solution (Beyotime) overnight. For SICM imaging, ≈ 20000 hDPSCs were seeded onto the gelatin-modified PDMS in a 40 mm cell culture petri dish containing 2 mL of α -MEM media. One day after seeding, the cell samples were washed three times with PBS solution, the α -MEM medium was replaced, and the cells were imaged using the SICM system. The topographic and current images were obtained using skip and approach-retract scan (ARS) dual modes. In this method, the nanopipette initially approaches the surface from a starting position D_{ps-max} . It then halts at D_{ps-min} when the current reduction surpasses a pre-defined set-point based on the sample surface. Once D_{ps-min} is reached, the probe retracts from D_{ps-min} back to D_{ps-max} . In a wide range of cellular morphology detection, the ΔI -based SICM system performs a coarse scan (64×32 pixels) and a fine scan (256×128 pixels) in a $40 \times 20 \mu m^2$ area within 20 mins. For probing the topography and extracellular charge distribution of cellular membrane, the system performs a coarse scan (32×32 pixels) and a fine scan (128×128 pixels) in a $5 \times 5 \mu m^2$ area in ≈ 8 min. To record the tip piezo and ionic current signal, a digital oscilloscope (Yokogawa DL950 scope reader) was utilized.

Data Collection and Analysis

Statistical analysis was performed using GraphPad Prism 8.0. All data are presented as the mean \pm standard deviation (SD) unless otherwise indicated. Data normality was assessed using the Shapiro-Wilk test ($n < 10$). For normally distributed data, comparisons between two groups were conducted using Student's t-test, and comparisons among multiple groups were performed using ANOVA followed by post hoc Bonferroni correction. A p-value of < 0.05 ($P < 0.05$) was considered statistically significant. During the scanning process, the oscilloscope recorded the time traces of z-piezo movement and ionic current, which were used for constructing ΔI images and for further analysis. The data analysis was performed using XEI (Park Systems), LabVIEW, and Origin Pro (OriginLab Corp.). Ionic current images were constructed using custom LabVIEW programs, while the 3D and 2D topography images were analyzed using XEI.

Supporting Information

Supporting Information is available from the Wiley Online Library or from the author.

Acknowledgements

Y.S. and S.Z. contributed equally to this work. This study was supported by the National Sciences Foundation of China (62001239), the National Natural Science Innovative Research Group Project (61821002), the Key Project of the National Natural Science Foundation of China (51832001), the Frontier Fundamental Research Program of Jiangsu Province for Leading Technology (BK20222002).

Conflict of Interest

The authors declare no conflict of interest.

Data Availability Statement

The data that support the findings of this study are available from the corresponding author upon reasonable request.

Keywords

aging cell, extracellular membrane imaging, finite element modeling, Scanning ion conductance microscopy

Received: September 27, 2023

Revised: November 21, 2023

Published online: December 10, 2023

- [1] M. J. Mitchell, M. M. Billingsley, R. M. Haley, M. E. Wechsler, N. A. Peppas, R. Langer, *Nat Rev Drug Discov* **2021**, 20, 101.
- [2] X. Zhang, G. Ma, W. Wei, *NPG Asia Mater.* **2021**, 13, 52.
- [3] H. Ida, N. Taira, K. Azuma, A. Kumatani, M. Akishiba, S. Futaki, Y. Takahashi, H. Shiku, *Electrochim. Acta* **2023**, 441, 141783.
- [4] I. Constantinou, E. E. Bastounis, *Trends Biotechnol.* **2023**, 41, 939.
- [5] D. Perry, B. Paulose Nadappuram, D. Momotenko, P. D. Voyias, A. Page, G. Tripathi, B. G. Frenguelli, P. R. Unwin, *J. Am. Chem. Soc.* **2016**, 138, 3152.
- [6] T. Banerjee, D. Biswas, D. S. Pal, Y. Miao, P. A. Iglesias, P. N. Devreotes, *Nat. Cell Biol.* **2022**, 24, 1499.
- [7] H. T. Baytekin, A. Z. Patashinski, M. Branicki, B. Baytekin, S. Soh, B. A. Grzybowski, *Science* **2011**, 333, 308.
- [8] X. Ma, M. Li, X. Xu, C. Sun, *Appl. Surf. Sci.* **2023**, 608, 155232.
- [9] S. M. Leitao, B. Drake, K. Pinjusic, X. Pierrat, V. Navikas, A. P. Nievergelt, C. Brillard, D. Djekic, A. Radenovic, A. Persat, D. B. Constam, J. Anders, G. E. Fantner, *ACS Nano* **2021**, 15, 17613.
- [10] F. Chen, J. He, P. Manandhar, Y. Yang, P. Liu, N. Gu, *Nanoscale* **2021**, 13, 19973.
- [11] C. Zhu, K. Huang, N. P. Siepser, L. A. Baker, *Chem. Rev.* **2021**, 121, 11726.
- [12] K. Cremin, B. A. Jones, J. Teahan, G. N. Meloni, D. Perry, C. Zeffass, M. Asally, O. S. Soyer, P. R. Unwin, *Anal. Chem.* **2020**, 92, 16024.
- [13] D. Wang, L. Sun, S. Okuda, D. Yamamoto, M. Nakayama, H. Oshima, H. Saito, Y. Kouyama, K. Mimori, T. Ando, S. Watanabe, M. Oshima, *Biomaterials* **2022**, 280, 121256.
- [14] A. S. Rubfaro, P. S. Tsegay, Y. Lai, E. Cabello, M. Shaver, J. Hutcheson, Y. Liu, J. He, *ACS Appl. Bio Mater.* **2021**, 4, 1632.
- [15] M. Miragoli, A. Moshkov, P. Novak, A. Shevchuk, V. O. Nikolaev, I. El-Hamamsy, C. M. F. Potter, P. Wright, S. H. S. A. Kadir, A. R. Lyon, J. A. Mitchell, A. H. Chester, D. Klenerman, M. J. Lab, Y. E. Korchev, S. E. Harding, J. Gorelik, *J. R. Soc., Interface* **2011**, 8, 913.
- [16] J. Rheinlaender, N. A. Geisse, R. Proksch, T. E. Schäffer, *Langmuir* **2010**, 27, 697.
- [17] V. Navikas, S. M. Leitao, K. S. Grussmayer, A. Descloux, B. Drake, K. Yserentant, P. Werther, D.-P. Herten, R. Wombacher, A. Radenovic, G. E. Fantner, *Nat. Commun.* **2021**, 12, 4565.
- [18] T. Ali, J. Bednarska, S. Vassilopoulos, M. Tran, I. A. Diakonov, A. Ziyadeh-Isleem, P. Guicheney, J. Gorelik, Y. E. Korchev, M. M. Reilly, M. Bitoun, A. Shevchuk, *FASEB J.* **2019**, 33, 8504.
- [19] G. Liu, L. Hao, H. Li, K. Zhang, X. Yu, D. Li, X. Zhu, D. Hao, Y. Ma, L. Ma, *Anal. Chem.* **2022**, 94, 5248.
- [20] L. Moreira Teixeira, L. Mezzanotte, *View* **2021**, 2, 20200177.

- [21] D. Zhang, L. Qiao, *View* **2022**, 4, 20220037.
- [22] R. Zhang, C. Rejeeth, W. Xu, C. Zhu, X. Liu, J. Wan, M. Jiang, K. Qian, *Anal. Chem.* **2019**, 91, 7078.
- [23] G. Caniglia, G. Tezcan, G. N. Meloni, P. R. Unwin, C. Kranz, *Annu. Rev. Anal. Chem.* **2022**, 15, 247.
- [24] E. Frömter, *The Journal of Membrane Biology* **1972**, 8, 259.
- [25] K. Mckelvey, S. L. Kinnear, D. Perry, D. Momotenko, P. R. Unwin, *J. Am. Chem. Soc.* **2014**, 136, 13735.
- [26] L. H. Klausen, T. Fuhs, M. Dong, *Nat. Commun.* **2016**, 7, 12447.
- [27] F. Chen, N. Panday, X. Li, T. Ma, J. Guo, X. Wang, L. Kos, K. Hu, N. Gu, J. He, *Nanoscale* **2020**, 12, 20737.
- [28] M. Keshavarz, K. Xie, K. Schaaf, D. Bano, D. Ehninger, *Mol. Psychiatry* **2022**, 28, 242.
- [29] J.-H. Chen, C. N. Hales, S. E. Ozanne, *Nucleic Acids Res.* **2007**, 35, 7417.
- [30] F. Rossiello, D. Jurk, J. F. Passos, F. d'Adda Di Fagagna, *Nat. Cell Biol.* **2022**, 24, 135.
- [31] X.-L. Liu, J. Ding, L.-H. Meng, *Acta Pharmacol. Sin.* **2018**, 39, 1553.
- [32] T. Liang, Z. Xing, L. Jiang, J. J. Zhu, *View* **2021**, 2, 20200131.
- [33] M. Al-Azab, M. Safi, E. Idiatullina, F. Al-Shaebi, M. Y. Zaky, *Cell. Mol. Biol. Lett.* **2022**, 27, 69.
- [34] Z. Qian, D. Ross, W. Jia, Q. Xing, F. Zhao, *Bioactive Materials* **2018**, 3, 167.
- [35] Y. J. Chuah, S. Kuddannaya, M. H. A. Lee, Y. Zhang, Y. Kang, *Biomater. Sci.* **2015**, 3, 383.
- [36] R. Kumari, P. Jat, *Frontiers in Cell and Developmental Biology* **2021**, 9, 485.
- [37] Y. Sang, X. Wen, Y. He, *View* **2022**, 3, 20220047.
- [38] Y. Ruzankina, A. Asare, E. J. Brown, *Mechanisms of Ageing and Development* **2008**, 129, 460.
- [39] J. Flach, S. T. Bakker, M. Mohrin, P. C. Conroy, E. M. Pietras, D. Reynaud, S. Alvarez, M. E. Diolaiti, F. Ugarte, E. C. Forsberg, M. M. Le Beau, B. A. Stohr, J. Méndez, C. G. Morrison, E. Passequé, *Nature* **2014**, 512, 198.
- [40] M. Ogrodnik, *Aging Cell* **2021**, 20, e13338.
- [41] N. M. Goldenberg, B. E. Steinberg, *Cancer Res.* **2010**, 70, 1277.
- [42] U. Zentgraf, A. G. Andrade-Galan, S. Bieker, *Cell. Mol. Biol. Lett.* **2022**, 27, 4.
- [43] X. Xing, H. Huang, X. Gao, J. Yang, Q. Tang, X. Xu, Y. Wu, M. Li, C. Liang, L. Tan, L. Liao, W. Tian, *ACS Appl. Mater. Interfaces* **2022**, 14, 3885.
- [44] Z. Liu, Y. Song, D. Li, *J. Colloid Interface Sci.* **2020**, 578, 116.